CARBON NANOTUBES: OPTICAL and EXCITONIC PROPERTIES†

Article for Dekker Encyclopedia of Nanoscience and Nanotechnology

R. Saito,* [1] M.S. Dresselhaus,‡ G. Dresselhaus,‡‡ A. Jorio,# A. G. Souza Filho,## and M. A. Pimenta,#

*** Department of Physics, Tohoku University, Sendai, 980-8578 Japan**

‡ Department of Electrical Engineering and Computer Science and Department of Physics, Massachusetts Institute of Technology, Cambridge, MA 02139 USA

‡‡Francis Bitter Magnet Laboratory, Massachusetts Institute of Technology, Cambridge, MA 02139 USA

 # Departamento de Física, Universidade Federal de Minas Gerais, Belo Horizonte, MG, 30123-970 Brazil

Departamento de Física, Universidade Federal do Ceará, Fortaleza - CE, 60455-900 Brazil

(Draft of December 4, 2012)

* **Author to whom correspondence should be addressed**

Keywords: nanotubes, Raman spectroscopy, excitons, resonance Raman, double resonance, Van Hove singularity, density of states, trigonal warping effect, Kohn anomaly, photoluminescence, chiral vector

Overview

The interaction between light and solids gives rise to many optical phenomena that can be observed by a variety of experimental techniques such as: (1) photo (or infrared) absorption and emission, (2) Raman and Rayleigh scattering, (3) photo-electron and Auger

[1] Riichiro Saito is a Professor of Physics at Tohoku University, Japan and has worked intensively on the theory of carbon nanotubes since 1991. E-mail: rsaito@flex.phys.tohoku.ac.jp

spectroscopy, (4) ultra-violet and X-ray photo-electron spectroscopy, etc[1]. Especially for single wall carbon nanotubes (SWNTs), that is, a graphene sheet rolled up into a seamless cylinder with a diameter around 1-3nm and a length of more than one micron[2], much useful information on the optical properties can be obtained by exploiting low-dimensional effects in which electrons and phonons are confined and coupled to each other in a one dimensional (1D) system. In the 1D system, an exciton (a photoexcited electron-hole pair) is confined and thus the binding energy of the exciton of the SWNT becomes large ($\sim$ 1eV) compared with the exciton in three dimensional (3D) semiconductors ($\sim$ 1meV)[3]. Since the exciton exists in SWNTs at room temperature, most of the optical properties, such as observed by their resonance Raman behavior or by Rayleigh scattering spectra, the electron-phonon interaction for phonons (the Kohn anomaly) and the electron-electron interaction (electronic Raman spectra) are described by the exciton picture[4]. In this article, which is an updated version of the encyclopedia article published in 2002, we overview the optical properties based on exciton photophysics, which was in a great progress during this decade.

Since an exciton is localized in real space, an exciton wavefunction is expressed by a linear combination of delocalized Bloch states specified by the wavevector k, in which the contribution of each k state to an exciton wavefunction, $Z(k)$, is given by solving the Bethe-Salpeter equation[5]. Once we know $Z(k)$, the exciton-photon or exciton-phonon interactions can be expressed by a linear combination of electron-photon or electron-phonon interactions, respectively, in k space by appropriate weighting of $Z(k)$ [6]. Electron-photon or electron-phonon interactions are calculated as a function of k by use of extended tight binding methods within a single particle picture. Thus the optical properties of the ex-

citon can be calculated by considering exciton-photon and exciton-phonon interactions, which depend on the geometric structure of a SWNT. In this article, we will not go into detail regarding the derivation of the exciton-photon and exciton-phonon interactions, but we will instead discuss the experimental observations and compare them with the calculated results.

Chiral vector: definition of a SWNT

First of all, we define the geometrical structure of a SWNT. In Fig. 1 we show the cylindrical structures of SWNTs. Each end of the nanotube is terminated by the hemisphere of a fullerene, or a cap, containing six pentagonal carbon rings. Since it is considered that nanotubes grow with a cap, the cap structure is essential for generating different kinds of geometries for nanotubes. However, since a SWNT is usually sufficiently long (micron) compared with the SWNT diameter (nm), we will neglect the effect of caps for discussing the optical properties.

Among the various nanotube structures, there are only two kinds of nanotubes which have mirror symmetry along the nanotube axis, namely the armchair and zigzag nanotubes, as shown in Fig. 1(a) and (b), respectively. The names of armchair and zigzag are taken from the shape of the edge cuts shown on the right side of Fig. 1. All other nanotubes [Fig. 1(c)] exhibit axial chirality and are called chiral nanotubes.

The geometry of a nanotube is uniquely expressed by two integers, (n, m). In Fig. 2, the rectangle OAB′B is shown, and by connecting OB to AB′, we can make the cylindrical shape of the nanotube. In this case, the vector OA (hereafter we call OA the chiral vector) corresponds to the equator of the nanotube. OA can be expressed by a linear combination

of the two unit vectors $\mathbf{a_1}$, and $\mathbf{a_2}$, of the honeycomb lattice shown in Fig. 2, so that

$$\mathrm{OA} = n\mathbf{a_1} + m\mathbf{a_2} \equiv (n, m). \tag{1}$$

The length of OA divided by π gives the diameter of the nanotube, d_t. Two lattice vectors OB and AB′, which are perpendicular to OA, correspond to the translation vector $\mathbf{T}$, in the one-dimensional lattice of the nanotube, and $\mathbf{T}$ is a function of n and m, as shown in Table 1. The rectangle OAB′B denotes the unit cell of the nanotube containing N hexagons and $2N$ carbon atoms, where N is expressed by

$$N = \frac{2(n^2 + m^2 + nm)}{d_R}. \tag{2}$$

The integer d_R is the greatest common divisor (gcd) of $(2n + m)$ and $(2m + n)$. Further details of the mathematics describing these variables are given in Table 1 and are further explained in Reference[2].

Fig.1 and 2 Table 1

Cutting lines: one dimensional Brillouin zone

The valence electrons of sp^2 carbons, such as graphite and nanotubes, consist of π (2p) electrons. Since each carbon atom in a nanotube has one π electron (and since there are $2N$ carbon atoms in the nanotube unit cell), $2N$ one-dimensional electronic π bands are obtained for a SWNT by applying periodic boundary conditions around the circumferential direction OA. Such a treatment for the electronic structure is called "zone-folding." Along the direction OA, the wavevectors (2π/(wave length)) which are perpendicular to the nanotube axis direction, $\mathbf{k}_\perp$, are discrete and are given by the condition:

$$\mathbf{C_h} \cdot \mathbf{k}_\perp^{\mathbf{p}} = 2\pi p, \quad (p = 1, \ldots, N). \tag{3}$$

Thus one obtains N inequivalent $\mathbf{k}_{\perp}^{\mathbf{p}} = 2\pi p/|C_h| = 2p/d_t$ discrete wave vectors for bonding and anti-bonding π bands, and the one-dimensional wave vectors, $\mathbf{k}_{\parallel}$, parallel to the nanotube axis, are continuous ($-\pi/T < k_{\parallel} < \pi/T$) for an infinitely long SWNT. The one dimensional Brillouin zone thus obtained is called a cutting line. When we discuss the electronic or phonon structure of a SWNT, the concept of the cutting lines is important[7, 8].

Electronic structure of a SWNT

One-dimensional energy dispersion relations for a nanotube $E_{1D}(p, k_{\parallel})$ are obtained by cutting the two-dimensional energy dispersion relations of graphite $E_{2D}(k)$ along the $\mathbf{k}_{\parallel}$ direction with wave vectors $k_{\perp}^{p}$ placed at equal distances of $2/d_t$ with a length of $2\pi/T$,

$$E_{1D}(p, k_{\parallel}) = E_{2D}(\mathbf{k}_{\perp}^{\mathbf{p}} + \mathbf{k}_{\parallel}) \tag{4}$$

where, by a tight binding calculation, $E_{2D}(k)$ is given by:

$$E_{g2D}(k_x, k_y) = \pm\gamma_0 \left\{ 1 + 4\cos\left(\frac{\sqrt{3}k_x a}{2}\right)\cos\left(\frac{k_y a}{2}\right) + 4\cos^2\left(\frac{k_y a}{2}\right) \right\}^{1/2} \tag{5}$$

in which the coordinates of k_x and k_y are given in Table 1. The plus and minus signs in Eq. (5) correspond to unoccupied (anti-bonding) and occupied (bonding) π energy bands, respectively. Here $\gamma_0 > 0$ is the tight binding nearest neighbor overlap energy parameter. When we plot the E_{g2D} in the hexagonal 2D Brillouin zone (see Fig. 3), the bonding and anti-bonding energy dispersion relations touch each other at the hexagonal corners, which are the K and K' points of the two-dimensional Brillouin zone (BZ). Because of the periodicity of $E_{g2D}(k_x, k_y)$ in k space, the K and K' points are inequivalent to each other, which we call the K and K' valleys. For Raman scattering in SWNTs, there are two

kinds of scattering processes, that is, intravalley and intervalley scattering processes in which the photo-electrons are scattered, respectively, within the same valley and between different valleys (K $\rightarrow$ K') .

The asymmetry between the shapes of the bonding and anti-bonding π bands comes not directly from Eq. (5) but rather from the higher order corrections to the tight binding parameters known as the overlap parameter s. In the following discussion, however, for simplicity, we use $s = 0$, since the value of s that we used is small ($s = 0.129$). Fig.3 and 4

Cutting these 2D energy dispersion relations by equi-distant lines parallel to the nanotube axis (cutting lines) corresponds to obtaining the 1D energy dispersion of nanotubes, as shown in Fig. 4. In this formulation, the Fermi energy is located at $E = 0$, and thus depending on whether there are energy bands which cross the Fermi energy or not, the nanotube is, respectively, either metallic or semiconducting. The condition to get either metallic or semiconducting nanotubes is whether the cutting lines cross the K or K' points where the bonding and anti-bonding π bands of 2D graphite touch each other (see Fig. 3). Fig.5

In Fig. 5 we show by solid lines the electronic density of states (DOS) for (a) (10,0) and (b) (9,0) zigzag nanotubes. Dotted lines denote the DOS for two-dimensional graphite for comparison. For metallic nanotubes, the density of states at the Fermi energy is constant as a function of energy, while there is an energy gap for semiconducting nanotubes as seen in Fig. 5. The value of the density of states at the Fermi energy, $D(E_F)$, is $8/\sqrt{3}\pi a\gamma_0$ in units of states per unit length along the nanotube axis per eV and $D(E_F)$ is independent of diameter. If $D(E_F)$ is given by per gram per eV, the $D(E_F)$ is relatively large for small diameter nanotubes. The many spikes in a plot of the DOS vs. energy for nanotubes correspond to the energy positions of the minima (or maxima) of the energy dispersion

curves of Fig. 4. Each spike exhibits a singularity of $1/\sqrt{E-E_0}$ (where E_0 is the energy extremum) that is characteristic of one-dimensional materials and this singularity is known as a Van Hove singularity.

Van Hove singularity

The energy position of the Van Hove singularity near the Fermi energy is determined by how the cutting lines are located near the K point of the 2D BZ. Since the wavefunctions have a time-reversal symmetry between K and K', the relative position of the cutting lines to the K' point is the same as that to the K point. Thus the Van Hove singular energies are degenerate for the K and K' valleys. When a magnetic flux unit goes through a hollow core of a nanotube cylinder, this degeneracy is lifted[2]. Fig.6

In Fig. 6 we show the cutting lines around the K point for (a) metallic and (b) semiconducting nanotubes. In the case of metallic nanotubes, the central cutting line just goes through the K point, and the two nearest cutting lines are located at the same distance of $\mathbf{K}_2$ from the K point. The corresponding energy dispersions for the central cutting line and for the two neighboring lines are, respectively, metallic linear energy dispersions, and are the first subbands (see Fig. 4a) which give the van Hove singularities, E_{11}^{M} nearest to the Fermi energy. An important fact about the energy dispersion of 2D graphite (known as graphene) around the K point is that the energy dispersion of Eq. (5) is linear in wavevector k, when we measure k from the K point, that is

$$E(k) = \pm\frac{\sqrt{3}\gamma_0}{2}|k|a. \tag{6}$$

Within the linear approximation of the energy dispersion, the equi-energy contour of two-dimensional graphite is a circle around the K point (see Fig. 7). Thus only the distance of

the two neighboring cutting lines from the K point is essential for determining the energy position of a Van Hove singularity. Since the separation between two cutting lines, K_2, is inversely proportional to the diameter of the nanotube, d_t, the Van Hove singular energies relative to the Fermi energy, E_{11}^{M}, are inversely proportional to d_t, too. Fig. 7

In the case of a semiconducting nanotube, on the other hand, the K point is always located at a position one-third of the distance between the two cutting lines as shown in Fig. 6(b)[2]. Thus the first and the second Van Hove singular energies, E_{11}^{S} and E_{22}^{S}, respectively, correspond to the one-dimensional energy dispersion for the nearest and the second nearest cutting lines, respectively, whose energies, as shown in Fig. 6, are one-third and two-third of the smallest energy separation of the Van Hove singularity of metallic nanotubes with a similar diameter.

The Kataura plot

Fig. 8

In Fig. 8(a), the energy separations of E_{ii}^{S} and E_{ii}^{M} are plotted as a function of nanotube diameter, d_t, in which each point corresponds to a different (n, m) nanotube. We call this plot a Kataura plot because Kataura et al. were the first to make such a plot for explaining phenomena such as the three peak structure of the optical absorption spectra observed for a SWNT bundle. In such a plot, they assigned the three lowest energy transitions to E_{11}^{S}, E_{22}^{S}, and E_{11}^{M} [9]. The authors of this article have used this plot for obtaining the resonance condition of Raman spectra [10], and with such a plot we can even assign the nanotube chirality (n, m) from measurement of the Raman spectra of an individual single nanotube, as shown in Fig. 8(b) [11].

The Kataura plot has also been used for characterizing the diameter distribution of

a SWNTs sample by Raman spectroscopy. The Kataura plot itself has been improved by introducing the curvature effect by using the extended tight binding method [12] and by introducing the exciton and environmental effects [13]. The most updated Kataura plot information is now obtained on the "exciton Kataura plot page" at http://flex.phys.tohoku.ac.jp/eii/. By changing the laser excitation energy, we can also get the experimental Kataura plot, from Raman [14], photoluminescence [15], and coherent phonon spectroscopy[16].

Trigonal warping effect

The linear energy approximation, however, does not work well for k points far from the K point. In this case, the equi-energy contours become deformed with a deformation that increases with increasing k, and the contour eventually becomes a triangle which connects three M points around the K point (Fig. 7) when we consider the periodicity of the electron dispersion relations in k space. The distortions of the equi-energy contours for large k values shown in Fig. 7, are known as the trigonal warping effect of the energy dispersion [10]. When the trigonal warping effect is included in calculating the dispersion relations, the direction of the cutting lines, which depends on the chiral angle of the nanotube (or simply on its chirality), is essential to determine the precise positions of the Van Hove energies. For example, two neighboring cutting lines in the metallic nanotube in Fig. 6(a) are not equivalent to each other, and this fact gives rise to a splitting of the Van Hove peaks in the DOS. This splitting of Van Hove peaks is a maximum for zigzag nanotubes and monotonically decreases with chiral angle to zero for armchair nanotubes for which the two neighboring cutting lines are equivalent to each other. For both metallic and semiconducting nanotubes, the trigonal warping effect appears as a modification of

the energy position of the Van Hove singularities, that depends on chirality. This value of the splitting of the Van Hove singularities (0.1 eV at most) is large enough to be easily detected by the energy accuracy of resonance Raman spectroscopy (10 meV). It is therefore possible to specify the (n, m) values for SWNTs from a detailed analysis of the resonance Raman spectra of each SWNT using a tunable laser.

Resonance Raman spectroscopy

If the laser excitation energies are matched to an E_{ii} of a SWNT, the Raman intensity is enhanced by about a factor of 10^3, which is known as the resonance Raman effect and the spectra thus obtained are called resonance Raman spectra. The resonance effect is strong in the case of SWNTs, since the Van Hove singularity of the joint density of states is sharp ($1/\sqrt{E - E_{ii}}$). When the laser light is focused down to a diameter of about the wavelength by an optical microscope, we can observe the Raman signal with a spatial resolution of 1 micron, which we call a micro-Raman measurement. By scanning the light over the surface of the sample, we can get the spacial distribution of an (n, m) specified SWNT or of graphene, and obtaining the spacial distribution is called Raman mapping. For a fixed point of the laser light, when we change the energy of the laser light, a strong resonance Raman signal is obtained for each (n, m) SWNT around each E_{ii} energy, which is called the Raman excitation profile. In order to get a continuous laser light source, a dye laser excited by another laser is often used and a triple monochromater is used as an optical filter for efficiently removing the Rayleigh scattered light while getting good spectral resolution. When we put an isolated SWNT on the sample holder or when we use a sample with a low SWNT density (1-10 SWNTs / μm^2), it is very hard to observe

a resonance Raman signal.

Typical Raman vibrations of a SWNT that are seen in the Raman spectra are (1) the radial breathing mode (RBM, 100-400cm^{-1}) in which the diameter of a nanotube is vibrating, (2) the G band (longitudinal (LO) and in-plane transverse optic (iTO) modes, 1550-1580cm^{-1}) which is split into G+ and G− bands in the case of SWNTs, (3) the D band (1350cm^{-1}) which appears only for the case that SWNTs have defects, and (4) the G' band (or 2D band, 2700cm^{-1}) which is a two phonon mode as discussed further in the next section.

Single and double resonance Raman spectra

In an inelastic scattering process of light, one or several phonons can be excited. In one phonon generation, since the scattered state for the photo-excited electron from k to $k+q$ comes by $-q$ phonon emission, the photo-excited electrons should recombine with a hole forming an electron-hole pair; this process thus results in an emitted scattered photon, where the phonon $-q$ vector should be zero. Thus only a phonon frequency at the Γ point (center of the Brillouin zone) is observed in first order Raman scattering, which is a one-phonon Raman process. In a single resonance Raman spectra, either the incident photon or the scattered photon is resonant, having the same energy as that of the transition energy between the ground and the excited states of the electron. We call these processes incident or scattered resonance, respectively.

In the case of two phonon emission, the restriction of $q = 0$ for one-phonon Raman case is relaxed. Thus for two phonon-emission, any q can be selected as far as a pair of q and $-q$ phonon vectors must be selected to return to the original k states of the electron

for completion of a Raman process. In the second-order Raman process, there are three intermediate states, namely at the initial k, the intermediate $k+q$ and the final k for the photo-excited carriers. If two of the three intermediate states matches an actual electronic state, the Raman signal is enhanced twice in the sense that two of three factors in the energy denominators in the perturbation expansion of fourth order perturbation theory become zero, thereby resulting in a strong intensity, that is comparable to the intensity of a first order Raman process. This special second-order high intensity process is called double resonance Raman spectroscopy, because two of the three energy denominators vanish [17, 18].

In the case of SWNTs, the RBM and G bands are due to first order single resonance Raman spectral processes, while the G' and D bands are both second order double resonance Raman spectral features. For the double resonance Raman spectra, the G' band consists of two inelastically scattered phonons and the D band consists of an inelastic scattering by a phonon and an elastic scattering by a defect. There are many possible combination or overtone phonon modes that can be observed by double resonance Raman scattering, though the Raman spectral features other than G' and D band are generally weak because of their small electron-phonon interactions. For more discussion, see, for example, a review article and recent paper of double resonance theory[19, 20, 21].

The Kohn anomaly effect

Raman spectra are also observed when (1) applying pressure or uniaxial stress, (2) changing the temperature, (3) applying a magnetic field, and (4) changing the Fermi energy, and in each case valuable information about the electrons, phonons and the electron-phonon

interaction can be obtained. The electronic and phonon structures are both modified by applied fields and thus by measuring the Raman peak frequency and spectral width, we can determine the interaction between electrons and phonons. The Fermi energy can be changed, for example, by electro-chemical doping either through the use of an electrolytic solution or by applying a gate electrode on a SWNT. When the gate voltage is applied, an electric dipole layer appears around a SWNT which can change the Fermi energy by up to 1eV [22, 23].

If there is a metallic energy subband as occurs in a metallic SWNT or in graphene, a phonon can virtually excite a electron-hole pair in the metallic energy band by an electron-phonon interaction. Here "virtually" means that the electron-hole pair can be relaxed to emit a phonon again, which is a second-order perturbation for producing a phonon. As a result, the phonon frequency and the life time of the phonon is modified by the self-energy for a phonon coming from the electron-phonon interaction. Here the self-energy of a particle is defined by an increased energy (or mass) by emitting and by absorbing an elementary excitation virtually through an interaction of the particle with a field. In this case, the particle is a phonon, the excitation is the electron-hole pair generation, and the interaction is the electron-phonon interaction. As a result of this self-energy consideration, the phonon has both a different frequency from the so-called bare phonon frequency and a finite life time.

The real (imaginary) part of the phonon self energy corresponds to the frequency shifts (spectral broadening) of phonon spectra. In a general case, the phonon frequency decreases (softens) and the spectra becomes broad in the presence of the electron-phonon interaction with electron-hole pair formation at the metallic energy subband, which is the

Kohn anomaly effect [23]. The Kohn anomaly effect is a non adiabatic phenomena in the sense that the electron system can not remain in the ground state while it is involved in atomic vibration. In the adiabatic approximation, on the other hand, the electrons quickly follow the atomic vibration. The Kohn anomaly effect can be suppressed by changing the Fermi energy. More specifically, when the Fermi energy increases (or decreases) by half of the phonon energy, an electron-hole pair can not be excited by a phonon because of energy momentum conservation considerations and then the phonon softening phenomena do not appear [24].

Hereafter, we first discuss some specific subjects that are relevant to the optical properties of SWNTs. First we define the exciton and excitonic phenomena, which is followed by a discussion of modifications to the simple single and double resonance Raman spectra by self-energy considerations.

Exciton photophysics: Fluorescence

Optical emission or fluorescence signals from a nanotube are not easy to observe, because most SWNT samples contain bundles of nanotubes in which on average one of three nanotubes are metallic. In a metallic nanotube, the electron-hole recombination occurs non-radiatively through metallic energy dispersion pathways discussed above. Furthermore, optical or direct coupling between nanotubes in a bundle suppresses fluorescence in semiconducting nanotubes, but if a semiconducting nanotube is isolated from other nanotubes, it is then possible to measure fluorescence behavior. Such spectra have been obtained for nanotubes separated from one another in a zeolite or when nanotubes are coated by a micelle (soap) structure[15, 25]. The fluorescence of nanotubes occurs at the

real energy gap E_{11}^S of semiconducting nanotubes and provides a good probe of excitonic effects in SWNTs as discussed below. If high spatial resolution greater than the average distance between two nanotubes is available, we can assign (n, m) values from the fluorescence measurement on an individual nanotube[26].

Definition of an exciton

When we discuss optical processes for SWNTs, the concept of the exciton, which is defined as a bound pair of a photo-excited electron and a hole is important [5, 6, 27, 28, 29, 30, 31]. In conventional semiconductors, an exciton exists only at low temperatures below 10 K because the electron-hole interaction is relatively weak ($\sim$ 1meV). However, due to the low dimensionality of SWNTs, the overlap between the electron and the hole wavefunctions increases and the exciton binding energy for a SWNT become very large, up to 1eV. As a consequence, the exciton can exist in SWNTs even at the room temperature.

Because of the localization of the wave-function in real space, the delocalized Bloch wave-functions labelled by the wave-vector k become mixed with each other by the Coulomb interaction, and the mixing effect is solved in term of the Bethe Salpeter equation [5]. Since the exciton wavefunction has a Gaussian shape along the nanotube axis direction, the k dependent mixing coefficient, $Z(k)$, shows a Gaussian distribution whose center is at a Van Hove singular k point. Since the size of the exciton wavefunction is larger than the diameter d_t of a SWNT (around 1-10nm depending on d_t), the mixing coefficient has a large value for only one cutting line of the 1D Brillouin zone. For this reason the wavefunction is almost constant around the circumferential direction of a nanotube.

Generally speaking, an electron or a hole can exist on one of the two energy dispersion

curves around the degenerate Fermi energy, near the K and K' points in two dimensional Brilloin zone. Therefore, there are four possibilities (16 if we include spin) for the excitonic states, except for armchair tubes, which have 16 different excitons without considering spin because of their two-fold degenerate cutting lines for each K (K') point. However, because of symmetry consideration, three of the four excitonic states are not optically allowed, and these optically forbidden states are called dark excitons. Therefore only one of the four excitons is dominant, and is optically allowed (called the bright exciton) [32, 33].

Many body effects on the optical transition energies

The optical transition energies E_{ii} in the Kataura plot are given by the exciton energy. However, the Coulomb effect appears not only for electron-hole pairs but also for photo-excited electrons as well as for many valence electrons, and we call all of these additional effects collectively "many body effects". These latter interactions increase the energy of the electron (decrease the energy of a hole), and these energy contributions collectively contribute to increasing the energy gap compared with the single particle energy difference between an electron and a hole. This energy difference is called the self-energy correction of the Coulomb interaction.

In the first principles calculations, the self-energy correction is taken into account as a pseudo-particle energy. Here because of electron-electron interactions, the wavevector k in the lattice is no longer a good quantum number and therefore the excited electron has a life time for having a k. Thus the electron is treated as a pseudo-particle within its life time and an energy uncertainty for the pseudo-particle energy is thus introduced.

The exciton excitation energy is as a result given by E_{ii} = (single particle energy) + (self energy) - (exciton binding energy) $\equiv$ (pseudo particle energy) - (exciton binding energy). We call the (self energy) - (exciton binding energy) the many body effect [3, 5].

Measuring E_{ii} with photoluminescence

Because of the localization of the exciton wavefunction, optical transition matrix elements for an exciton are enhanced by a factor of 10^2 in comparison to the matrix element for a free electron-hole pair. This enhancement contributes to the possibility of observing single SWNT Raman and PL spectroscopy. This section deals with a review of the experimental work devoted to measuring the bright excitons for each (n, m) SWNT. The plot of these optical energies (E_{ii}) as a function of tube diameter (Fig. 8) has been called the "Kataura plot", in recognition of the importance of such plots for visually first introduced by H. Kataura et al.[34]. Fig.9

In the photoluminescence (PL) process, photo-absorption occurs at higher optical transition energies (E_{ii}, with $i > 1$), most generally E_{22} for a conventional range of experimental wavelengths, and the photo-excited carrier is rapidly relaxed to E_{11}. PL then occurs by the electron-hole recombination resulting in the emission of a photon with energy E_{11}. By building a two-dimensional map of the PL intensity as a function of the energies of the photo-absorption, many peaks appear corresponding to the pairs [E_{11} and E_{22}] for each (n, m) [35, 36]). Early historic work of single nanotube spectroscopy (Fig. 8) showed that different nanotube samples contained different (n, m) distributions, summarizing experimental data and for making comparisons to theoretical calculations[13]. The energy and intensity of these peaks (as illustrated in the Fig. 9 [35] for different wrapping media)

depend on environmental effects introduced by the nanotube coating which we discuss in the next subsection.

PL measurements provide a convenient and powerful tool for determining the distribution of (n, m) *semiconducting* SWNTs in the sample (Fig. 9a). Metallic SWNTs, however, do not exhibit any PL spectra, since the photo-excited carrier can decay non-radiatively at a much faster rate than the radiative decay into the metallic energy band. Thus in a SWNTs bundle, we expect a rapid energy transfer from a semiconducting SWNT to a metallic SWNT, so that no PL emission is observed in this case. Thus single SWNTs that are isolated by a surfactant or suspended between two electrodes in the air are needed to observe PL. These limitations can, however, be overcome by using resonance Raman spectroscopy which is discussed in the next Section.

Environmental effects

The optical properties of carbon nanotubes have been exploited for many applications and one common feature for all these applications is that the carbon nanotubes are functionalized by interaction with some specially tailored environment. Understanding how the interactions with the environment affect the optical properties is given by use of the exciton energy concept. Fig. 10

The measured E_{ii} values can be modified by dielectric constants of surrounding materials, which we call environmental effects. Figure 10 shows a comparison between the E_{ii} measured from two different samples, named the "super-growth" SWNT sample (bullets) [37] and the "alcohol-assisted" SWNT samples (open circles) [38]. From Fig. 10, we see that the $E_{ii}^{\rm exp}$ values from the "alcohol-assisted" SWNTs are generally red shifted with

respect to those from the "super-growth" SWNTs.

More generally, the E_{ii} energy upshifts or downshifts depends on whether the semiconductor SWNTs are type I or type II, and on the both value of i in E_{ii}, and the SWNT diameter. The magnitude of the observed shift in energy depends on the dielectric constant of the environmental material. This situation is similar to the behavior of the exciton energy for the hydrogen atom, which depends on the dielectric constant by substituting e^2/ϵ for e^2 in $me^4/2\hbar^2$ (1 Rydberg) term into the expression for the energy of the hydrogen 1s orbital. The contribution coming from the electric field between the e-h pair of the exciton that lies outside of the SWNT will also affect the exciton energy. Since the electric field also penetrates into the nanotube itself, the dielectric response of the π electron is also important. An important point is that even a metallic SWNT has an exciton binding energy, even though the perturbation due to the excitonic effects is relatively small in comparison to that of semiconducting SWNTs [29].

Assuming that κ_{tube} does not change from sample to sample, since the structure of a given (n, m) tube should be the same, these results indicate that the "alcohol-assisted" SWNTs are surrounded by a larger κ_{env} value than the "super-growth" SWNTs, thus increasing the effective κ and decreasing E_{ii} for the "alcohol-assisted" SWNTs. However, the general dielectric constant depends on the tube (n, m) structure. By "general" we mean κ comprises the screening from both the tube and the environment. Interestingly, d_t-dependent effective κ values for the exciton calculation are needed to reproduce the experimental E_{ii} values consistently[13].

Radial Breathing Mode

One of the most powerful optical measurements for carbon nanotubes is resonance Raman spectroscopy. The resonance enhancement effect, which is caused when the incident or scattered photon is in resonance with optical transitions involving Van Hove singularities in the valence and conduction band, allows the observation of a signal from even one nanotube, as shown in Fig. 8(b). Recently much progress in Raman spectroscopy has been made, and therefore it is not possible to cover all important advances in detail [see Reference 4] within the available space of this review. The present summary therefore only provides an overview of Raman spectroscopy of carbon nanotubes, and only a few essential points which are important for analyzing the many features of the resonance Raman spectra of SWNTs are discussed. Fig. 10

In carbon nanotubes, the Raman spectra show a variety of features associated with first-order processes, as well as combination or overtone modes up to $3200\,\mathrm{cm}^{-1}$ or even higher numbers (energy). The characteristic mode that is not observed in other sp^2 carbons but is only observed in nanotube samples is the radial breathing mode, RBM (see Fig. 10). The RBM frequency appears from 100–$550\,\mathrm{cm}^{-1}$, depending on the SWNT diameter, ranging from 2 nm–0.4 nm, respectively. In order to check if a sample contains single or double-wall nanotubes, the RBM spectra provides an easy way to do just that. It is noted that if no RBM spectra are observed, this does not always mean that there are no SWNTs in the sample, because we can imagine the case that the resonance condition for a given diameter distribution of SWNTs might be far from the available laser excitation energies. In some cases, because of the large signal from the wings of the Rayleigh (elastically) scattered light, the RBM signal cannot be resolved in the noisy Rayleigh

background signal. Use of a triple-monochromator or a notch filter is a simple way to avoid this problem, but use of a notch filter in practice limits observations to $\omega_{\rm RBM} > 100\,{\rm cm}^{-1}$.

In Fig. 11(b) we plot E_{ii} as a function of inverse tube diameter $1/d_t$. Circles and crosses correspond, respectively, to metallic and semiconducting (n,m) tubes. For a laser energy of 1.58 eV, only few metallic and semiconducting (n,m) tubes with E_{11}^M and E_{22}^S Van Hove singularities satisfy the resonance condition, as seen in Fig. 11(a). Since the resolution of a Raman spectra is typically of $1\,{\rm cm}^{-1}$ out of 100–200 $\rm cm^{-1}$, the difference between the peak frequencies of different (n,m) tubes can be easily distinguished. Fig. 11

G-band

The second important Raman feature is the G-band mode which appears near $1590\,{\rm cm}^{-1}$ in SWNTs. This band comes from the Raman-active mode of sp^2 carbons (graphite), and thus all graphitic materials show this spectral feature. What is special in nanotubes is that the G-band splits into two most prominent peaks, denoted by G^+ and G^-. In fact, six (or three) phonon modes are active for chiral (or achiral) nanotubes in this phonon frequency region, but, among the Raman-active modes, two A (or A_{1g}) modes are the strongest and account for the two peaks, G^+ and G^-. Regarding the other four Raman-active modes, two have E_1 and two have E_2 symmetries (or two Raman-active modes E_{1g} or E_{2g} in the case of achiral tubes), and these E_1 and E_2 modes give rise to relatively weak Raman peaks. The presence of the E_1 and E_2 modes are mainly seen from the Lorentzian decompositions of the lineshape of the observed spectra using polarized light when carrying out polarization studies. The difference between the two G band components, $G^+ - G^-$, is inversely proportional to d_t^2, which comes from the curvature

effect that is responsible for the splitting of the degenerate in-plane optic phonon modes, E_{2g}, of two-dimensional graphite at the Γ point [39].

D-band

In the range $1250-1400\,\mathrm{cm}^{-1}$, a defect-induced Raman feature , called the D-band, appears only for defective sp^2 carbons. The appearance of a strong D-band in nanotubes indicates that a nanotube has many symmetry-breaking defects. Nanotubes synthesized by different synthesis methods have varying degrees of defects. The D-band is a dispersive feature, since its frequency increases by approximately $50\,\mathrm{cm}^{-1}$ with a $1\,\mathrm{eV}$ increase in the laser excitation energy, E_{laser}. The physical origin of this very large dispersiveness has been explained by double resonance Raman theory [40, 41, 18] in which the photon-absorbed electron is scattered twice before final recombination. Although this process is a second-order light scattering process, the intensity is comparable to that of the first-order resonance process when two of the three intermediate states are in resonance with the real electronic states.

In Fig. 12 two different (a) first-order and (b) second-order Raman processes are shown. The crossed lines for each figure denote the electronic energy states of graphite around the K points in the Brillouin zone about which the optical transition occurs. The upper figure is for the incident laser light resonance condition in which the laser excitation is at almost the same energy as the energy required for optical absorption. The lower figure is for the scattered resonance condition, in which the scattered electron energy, $(E_{\mathrm{laser}} - E_{\mathrm{phonon}})$, is the same as the optical emission energy. The resonance laser energy differs in the two cases by the phonon energy. More precisely, the laser energy for the

scattered resonance energy is higher by E_{phonon} than that for the incident resonance energy in a Stokes scattering process which creates a phonon. An important point to be noted is that, for all Raman-active phonon modes, the incident resonance condition gives the same resonance laser energy, while the scattered resonance condition gives different laser energies, depending on the energy of phonons. Thus by observing more than one Raman spectral feature for the same tube or not, respectively, we know whether the observed resonance Raman process is with an incident photon or with a scattered photon.

In a first-order process, in order to recombine an electron and a hole at the original k point, the phonon wave vector q should be sufficiently small, or practically zero. This is why we see in most solid state textbooks that the Raman spectra of solids can be observed only for zone-center (q=0) Raman-active phonon modes. In the second-order, double or triple resonance process, it is clear from Fig. 12, that the phonon wave vector q is not zero. Furthermore, when the laser energy increases, the electron k vector becomes further apart from the K point in order to satisfy the requirements for optical absorption, and thus the corresponding q vectors become longer. Here we use the requirement of the double and triple resonance processes that the intermediate $k + q$ states should be unoccupied electronic states, too. This is the reason why the dispersive phonon modes change their Raman frequencies when the laser excitation energy is changed, since the phonon wave vector q that satisfies the double or triple resonance Raman condition changes when the excitation laser energy changes. Fig.12

Intravalley and Intervalley Scattering

In two-dimensional graphite, there are two inequivalent corners of the Brillouin zone, K and K', as shown in Fig.7, and also called Dirac points. In the electron scattering by phonons or impurities (elastic scattering), there are two possibilities. One is an intra-valley scattering process in which an electron (or the hole) scatters within the same region of the K (or K') point. The other is inter-valley scattering in which an electron (or a hole) is scattered from the K to the K' region (or K' to K). The corresponding phonon q vectors for intra-valley and inter-valley scattering are phonons around the Γ and K points, respectively. Thus we try to find the phonon dispersion point around either the Γ or K points which satisfies the double or triple resonance condition.

In Fig. 13(a) the phonon q vectors for the double resonance condition are shown as a function of $E_{\rm laser}$ (bottom axis) and of the q vector along $\Gamma - K$ (top axis). Solid and open circles correspond to phonon modes around the K and Γ points, respectively. In Fig. 13(b) are collected the many experimental Raman signals which have been observed in many disordered graphitic materials for many years, and these are here plotted in the Brillouin zone of 2D graphite [18]. By specifying either Γ or K point phonons, all of the experimental points could be assigned to one of the phonon energy dispersion relations (6 solid lines), thus providing clear evidence that double resonance theory can work well for the dispersive phonon modes of 2D graphite. The resulting dispersion relations show how resonance Raman scattering can be used to obtain phonon dispersion relations experimentally based on double resonance theory. Fig. 13

All second-order phonon processes shown here are one-phonon emission processes. Thus one of the two scattering processes shown in Fig. 12(b) should not be a phonon scat-

tering process. We consider that the non-phonon scattering process is an elastic electron scattering caused by an impurity or a defect in which electronic states with momentum k are mixed with each other. This is the reason why the dispersive phonon modes appear in a frequency region lower than $1620\,\mathrm{cm}^{-1}$ only for defective carbon materials. If the two scattering processes are both phonon scattering processes, we do not need the defect scattering process, and thus strong dispersive overtone phonon modes appear. An example of a two-phonon process is the G'-band appearing around $2700\,\mathrm{cm}^{-1}$ with its large dispersion of approximately $100\,\mathrm{cm}^{-1}/\mathrm{eV}$ [19].

k-dependent electron-phonon interaction

The measurement of double resonance Raman theory provides detailed information of scattering process. By changing the polarization direction of the light, we can we can change the k state of the photo-excited electron within the equi-energy contour of the two dimensional Brillouin zone. From this measurement, we can get information about inhomogeneous optical absorption in which the electron-photon matrix element is k dependent [42]. By changing the laser excitation energy, we can change the equi-energy contour for a photo-excited electron in the Brillouin zone, which is relevant to a double resonance scattering process[18, 19]. From this measurement, we can know which k of a photo-excited electron and which q of a phonon are relevant to the Raman intensity, thereby allowing researchers to fit the measured double resonance phonon energy to the calculated phonon dispersion relations[43]. Further, by changing the Fermi energy by electro-chemical doping, the phonon self-energy can be modified. From the gate-dependent Raman spectra, we can assign the phonon modes of for various combination phonon modes[44]. We cannot

here go into detail because of lack of space how to use these Raman techniques to obtain such microscopic pictures of phonon and electron-phonon interactions. The reader will learn from the recent publications on Raman spectroscopy that Raman spectroscopy not only provides a tool to measure the phonon frequency and corresponding lattice structure, but also allows fundamental understanding of detailed properties of optical processes[1].

Summary

In summary, the optical properties of carbon nanotubes shows rich spectra due to low dimensional physics phenomena, such as Van Hove singularities in the electronic density of states. The resonance Raman spectra, in particular, provide a powerful tool for observing individual nanotubes in the sample, and especially for specifying (n, m) values of individual nanotubes. Excitons in SWNTs are essential for understanding the detailed optical properties, such as environmental effects of the transition energy. Double resonance theory explains the dispersive Raman phonon modes such as the D and G' bands, and other double resonance Raman spectra can be used to provide detailed information about the phonon dispersion relations.

R.S. acknowledges a MEXT grant (No. 20241023) from the Ministry of Education, Japan. A.J. acknowledges financial support from "Rede Brasileira de Pesquisa e Instrumentação em Nano-Óptica" (CNPq). A.G.S.F. acknowledge support from INCT NanoBioSimes (CNPq-MCT) and PRONEX program (FUNCAP). The MIT authors acknowledge support under NSF Grant DMR 10-04147. M.A.P acknowledges the financial support from CNPq, the Brazilian Network on Carbon Nanotubes Research (CNPq), National Institute of Science and Technology of Carbon Nanomaterials (INCT/MCT/CNPq)

and NENNAM (PRONEX/F).

References

[1] Ado Jorio, Mildred S. Dresselhaus, Riichiro Saito, and Gene Dresselhaus, *Raman Spectroscopy in Graphene Related Systems* (Wiley-VCH Verlag GmbH & Co KGaA, WeinHeim, Germany, 2010).

[2] R. Saito, G. Dresselhaus, and M. S. Dresselhaus, *Physical Properties of Carbon Nanotubes* (Imperial College Press, London, 1998).

[3] M. S. Dresselhaus, G. Dresselhaus, R. Saito, and A. Jorio, Physics Reports **409**, 47 (2005).

[4] R. Saito, M. Hofmann, G. Dresselhaus, A. Jorio, and M. S. Dresselhaus, Advances in Physics **60**, 413 (2011).

[5] J. Jiang, R. Saito, Ge. G. Samsonidze, A. Jorio, S. G. Chou, G. Dresselhaus, and M. S. Dresselhaus, Phys. Rev. B **75**, 035407 (2007).

[6] J. Jiang, R. Saito, K. Sato, J. S. Park, Ge. G. Samsonidze, A. Jorio, G. Dresselhaus, and M. S. Dresselhaus, Phys. Rev. B **75**, 035405 (2007).

[7] Ge. G. Samsonidze, R. Saito, A. Jorio, M. A. Pimenta, A. G. Souza Filho, A. Grüneis, G. Dresselhaus, and M. S. Dresselhaus, Journal of Nanoscience and Nanotechnology **3**, 431 (2003).

[8] R. Saito, K. Sato, Y. Oyama, J. Jiang, Ge. G. Samsonidze, G. Dresselhaus, and M. S. Dresselhaus, Phys. Rev. B **72**, 153413 (2005).

[9] H. Kataura, Y. Kumazawa, Y. Maniwa, I. Uemezu, S. Suzuki, Y. Ohtsuka, and Y. Achiba, Synt. Met. **103**, 2555 (1999).

[10] R. Saito, G. Dresselhaus, and M. S. Dresselhaus, Phys. Rev. B **61**, 2981 (2000).

[11] A. Jorio, R. Saito, J. H. Hafner, C. M. Lieber, M. Hunter, T. McClure, G. Dresselhaus, and M. S. Dresselhaus, Phys. Rev. Lett. **86**, 1118 (2001).

[12] Ge. G. Samsonidze, R. Saito, N. Kobayashi, A. Grüneis, J. Jiang, A. Jorio, S. G. Chou, G. Dresselhaus, and M. S. Dresselhaus, Appl. Phys. Lett. **85**, 5703 (2004).

[13] A. R. T. Nugraha, R. Saito, K. Sato, P. T. Araujo, A. Jorio, and M. S. Dresselhaus, Appl. Phys. Lett. **97**, 091905 (2010).

[14] C. Fantini, A. Jorio, M. Souza, M. S. Strano, M. S. Dresselhaus, and M. A. Pimenta, Phys. Rev. Lett. **93**, 147406 (2004).

[15] M. J. O'Connell, S. M. Bachilo, X. B. Huffman, V. C. Moore, M. S. Strano, E. H. Haroz, K. L. Rialon, P. J. Boul, W. H. Noon, C. Kittrell, J. Ma, R. H. Hauge, R. B. Weisman, and R. E. Smalley, Science **297**, 593 (2002).

[16] Y. S. Lim, K. J. Yee, J. H. Kim, E. H Haroz, J. Shaver, J. Kono, S. K. Doom, R. H. Hauge, and R. E. Smalley, Nano Lett. **6**, 2696 (2006).

[17] C. Thomsen and S. Reich, Phys. Rev. Lett. **85**, 5214 (2000).

[18] R. Saito, A. Jorio, A. G. Souza Filho, G. Dresselhaus, M. S. Dresselhaus, and M. A. Pimenta, Phys. Rev. Lett. **88**, 027401 (2002).

[19] R. Saito, A. Grüneis, Ge. G. Samsonidze, V. W. Brar, G. Dresselhaus, M. S. Dresselhaus, A. Jorio, L. G. Cançado, C. Fantini, M. A. Pimenta, and A. G. Souza Filho, New Journal of Physics **5**, 157 (2003).

[20] M. A. Pimenta, G. Dresselhaus, M. S. Dresselhaus, L. G. Cançado, A. Jorio, and R. Saito, Physical Chemistry Chemical Physics **9**, 1276 (2007).

[21] P. Venezuela, M. Lazzeri, and F. mauri, Phys. Rev. B **84**, 035433 (2011).

[22] H. Farhat, H. Son, Ge. G. Samsonidze, S. Reich, M. S. Dresselhaus, and J. Kong, Phys. Rev. Lett. **99**, 145506 (2007).

[23] K. Sasaki, H. Farhat, R. Saito, and M. S. Dresselhaus, Physica E **42**, 2005 (2010).

[24] K. Sasaki, R. Saito, G. Dresselhaus, M. S. Dresselhaus, H. Farhat, and J. Kong, Phys. Rev. B **77**, 245441 (2008).

[25] Z. M. Li, Z. K. Tang, H. J. Liu, N. Wang, C. T. Chan, R. Saito, S. Okada, G. D. Li, J. S. Chen, N. Nagasawa, and S. Tsuda, Phys. Rev. Lett. **87**, 127401 (2001).

[26] S. M. Bachilo, M. S. Strano, C. Kittrell, R. H. Hauge, R. E. Smalley, and R. B. Weisman, Science **298**, 2361–2366 (2002).

[27] T. Ando, J. Phys. Soc. Jpn. **66**, 1066 (1997).

[28] T. G. Pedersen, Phys. Rev. B **67**, 073401 (2003).

[29] C. D. Spataru, Sohrab Ismail-Beigi, Lorin X. Benedict, and Steven G. Louie, Phys. Rev. Lett. **92**, 077402 (2004).

[30] H. Zhao and S. Mazumdar, Synth. Met. **155**, 250 (2005).

[31] M. S. Dresselhaus, G. Dresselhaus, R. Saito, and A. Jorio. In *Annual Reviews of Physical Chemistry Chemical Physics*, edited by S. R. Leone, J. T. Groves, R. F. Ismagilov, and G. Richmond, pages 719–747, Annual Reviews, Palo Alto, CA, 2007.

[32] E. B. Barros, R. B. Capaz, A. Jorio, Ge. G. Samsonidze, A. G.Souza Filho, S. Ismail-Beigi, C. D. Spataru, S. G. Louie, G. Dresselhaus, and M. S. Dresselhaus, Phys. Rev. B Rapid **73**, 241406(R) (2006).

[33] E. B. Barros, A. Jorio, Ge. G. Samsonidze, R. B. Capaz, A. G.Souza Filho, J. Mendez Filho, G. Dresselhaus, and M. S. Dresselhaus, Physics Reports **431**, 261 (2006).

[34] H. Kataura, A. Kimura, Y. Ohtsuka, S. Suzuki, Y. Maniwa, T. Hanyu, and Y. Achiba, Jpn. J. Appl. Phys. Pt.2-Letters **37**, L616 (1998).

[35] C. Fantini, J. Cassimiro, V. S. T. Peressinotto, F. Plentz, A. G. Souza Filho, C. A. Furtado, and A. P. Santos, Chem. Phys. Letters **473**, 96101 (2007).

[36] S. M. Bachilo, M. S. Strano, C. Kittrell, R. H. Hauge, R. E. Smalley, and R. B. Weisman, Science **298**, 2361 (2002).

[37] Paulo T. Araujo and Ado Jorio, Phys. Status Solidi B **245**, 2201 (2008).

[38] P. T. Araujo, S. K. Doom, S. S. Kilina, S. Tretiak, E. Einarsson, S. Maruyama, H. Chacham, M. A. Pimenta, and A. A. Jorio, Phys. Rev. Lett. **98**, 067401 (2007).

[39] A. Jorio, A. G. Souza Filho, G. Dresselhaus, M. S. Dresselhaus, A. K. Swan, M. S. Ünlü, B. Goldberg, M. A. Pimenta, J. H. Hafner, C. M. Lieber, and R. Saito, Phys. Rev. B **65**, 155412 (2002).

[40] A. V. Baranov, A. N. Bekhterev, Y. S. Bobovich, and V. I. Petrov, Opt. Spectrosk. **62**, 1036 (1987).

[41] C. Thomsen and S. Reich, Phys. Rev. Lett. **85**, 5214 (2000).

[42] A. Grüneis, R. Saito, Ge. G. Samsonidze, T. Kimura, M. A. Pimenta, A. Jorio, A. G. Souza Filho, G. Dresselhaus, and M. S. Dresselhaus, Phys. Rev. B **67**, 165402 (2003).

[43] D. L. Mafra, J. Kong, K. Sato, R. Saito, M. S. Dresselhaus, and P. T. Araujo, Phys. Rev. B 86, 195434 (2012).

[44] P. T. Araujo, D. L. Mafra, K. Sato, R. Saito, J. Kong, M. S. Dresselhaus, Sci. Rep., in press, (2012).

Figure Captions:

Fig. 1 Single wall carbon nanotubes. The ends of nanotubes are capped by fullerene hemispheres. (a) armchair nanotube (b) zigzag nanotube, and (c) chiral nanotube. Fig. 2 The unrolled honeycomb lattice of a nanotube. OA is the equator of the nanotube and OB corresponds to the translation vector of this one-dimensional material and OA is the chiral vector. By connecting OB to AB′, we can make a seamless cylindrical shape. OAB′B is a unit cell of the nanotube. The figure corresponds to the (4,2) chiral nanotube and there are $N = 28$ hexagons in the unit cell for the nanotube.

Fig. 3 The energy dispersion relations for 2D graphite are shown throughout the whole region of the Brillouin zone. The inset shows the energy dispersion along the high symmetry points.

Fig. 4 The energy dispersion relations for carbon nanotubes, shown explicitly for the (a) (5,5) armchair, (b) (9,0) zigzag, (c) (10,0) zigzag nanotubes. Bold and thin lines are doubly or singly degenerate energy bands, respectively. The Fermi energy is located at $E = 0$. (5,5) and (9,0) are metallic nanotubes, while (10,0) is semiconducting.

Fig. 5 Electronic density of states for the: (a) (10,0) semiconducting zigzag nanotube, and the (b) (9,0) metallic zigzag nanotube. Dotted lines denote the density of states for two-dimensional graphite.

Fig. 6 Cutting lines around the K point in the Brillouin zone for (a) metallic and (b) semiconducting nanotubes.

Fig. 7 Equi-energy contours for the electronic π-bands of two-dimensional graphite.

Fig. 8 (a) Energy separations E_{ii} between valence and conduction band Van Hove singularities are plotted as a function of nanotube diameter for both semiconducting and

metallic SWNTs. (b) Raman spectra (radial breathing mode) from three different (n, m) isolated single wall nanotubes [10, 11].

Fig. 9 Photoluminescence excitation (PLE) maps of carbon nanotube samples dispersed in aqueous solution and wrapped with the following chemical moieties: (a) SDS, (b) NaDDBS, (c) NaC, and (d) DNA(GT)10. The same color scale for intensities, normalized to 1, were used in the four plots better visualization [35].

Fig. 10 $E_{ii}^{\rm exp}$ vs. $\omega_{\rm RBM}$ results obtained for the "super-growth" (bullets) and "alcohol assisted" (open circles) SWNT samples.

Fig. 11 Van Hove singular energies in the JDOS, E_{ii} as a function of $1/d_t$ are shown in (b) where circles and crosses correspond, respectively, to metallic and semiconducting nanotube with (n, m) chirality tubes. For 1.579 eV laser excitation, expansion of the rectangular section in (b) is shown in (a). The resonance condition satisfies only a limited number of (n, m) tubes whose RBM frequencies can almost always be distinguished from one another.

Fig. 12 (a) First-order Raman processes which are resonant with (a1) the incident and (a2) the scattered laser light. Solid and open dots denote resonance and non-resonance scattering processes, respectively. Crossed lines show the linear energy dispersion of 2D graphite around the K point. (b) Second-order Raman processes which are resonant the incident laser light in (b1,b2), and the scattered laser light in (b3,b4). The solid scattered vectors and dashed scattered vectors with wavevector q, respectively, denote inelastic and elastic scattering processes.

Fig. 13 (a) Calculated Raman frequencies for the double resonance condition as a function of $E_{\rm laser}$ (bottom axis) and q vector along $\Gamma - K$ (top axis). Solid and open

circles correspond to phonon modes around the K and Γ points, respectively. (b) The 6 graphite phonon dispersion curves (lines) and experimental Raman observations (symbols) are identified according to double resonance theory.

Table 1 Parameters for Carbon Nanotubes.[a)]

symbol	name	formula	value
a	length of unit vector	$a = \sqrt{3}a_{\mathrm{C-C}} = 2.49$ Å,	$a_{\mathrm{C-C}} = 1.44$ Å
$\mathbf{a}_1$,$\mathbf{a}_2$	unit vectors	$\left(\frac{\sqrt{3}}{2}, \frac{1}{2}\right)a,\ \left(\frac{\sqrt{3}}{2}, -\frac{1}{2}\right)a$	x, y coordinate
$\mathbf{b}_1$, $\mathbf{b}_2$	reciprocal lattice vectors	$\left(\frac{1}{\sqrt{3}}, 1\right)\frac{2\pi}{a},\ \left(\frac{1}{\sqrt{3}}, -1\right)\frac{2\pi}{a}$	k_x, k_y coordinate
$\mathbf{C}_h$	chiral vector	$\mathbf{C}_h = n\mathbf{a}_1 + m\mathbf{a}_2 \equiv (n, m), \quad (0 \le \lvert m\rvert \le n)$	
L	length of $\mathbf{C}_h$	$L = \lvert\mathbf{C}_h\rvert = a\sqrt{n^2 + m^2 + nm}$	
d_t	diameter	$d_t = L/\pi$	
θ	chiral angle	$\sin\theta = \frac{\sqrt{3}m}{2\sqrt{n^2 + m^2 + nm}}$	$0 \le \lvert\theta\rvert \le \frac{\pi}{6}$
		$\cos\theta = \frac{2n + m}{2\sqrt{n^2 + m^2 + nm}}, \quad \tan\theta = \frac{\sqrt{3}m}{2n + m}$	
d	gcd(n,m)[b)]		
d_R	gcd($2n + m$,$2m + n$)[b)]	$d_R = \begin{cases} d & \text{if } (n - m) \text{ is not multiple of } 3d \\ 3d & \text{if } (n - m) \text{ is multiple of } 3d \end{cases}$	
$\mathbf{T}$	translation vector	$\mathbf{T} = t_1\mathbf{a}_1 + t_2\mathbf{a}_2 \equiv (t_1, t_2)$	$\gcd(t_1, t_2) = 1$[b)]
		$t_1 = \frac{2m + n}{d_R},\ t_2 = -\frac{2n + m}{d_R}$	
T	length of $\mathbf{T}$	$T = \lvert\mathbf{T}\rvert = \frac{\sqrt{3}L}{d_R}$	
N	Number of hexagons in the nanotube unit cell.	$N = \frac{2(n^2 + m^2 + nm)}{d_R}$	

[a)] In this table n, m, t_1, t_2, p, q are integers and d, d_R N and M are integer functions of these integers.

[b)] $\gcd(n, m)$ denotes the greatest common divisor of the two integers n and m.

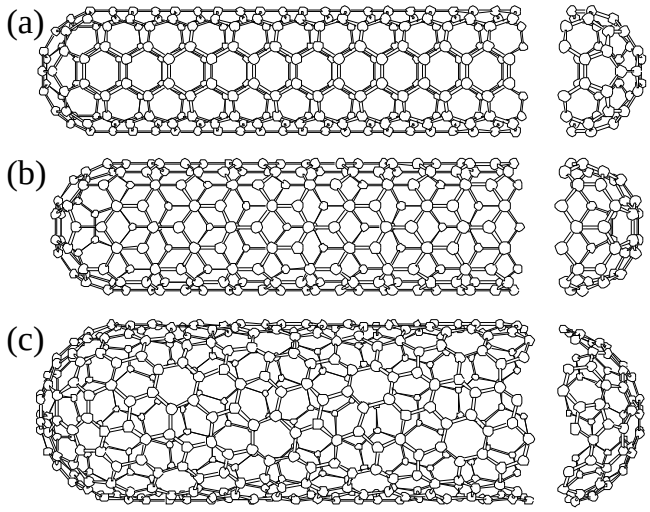

Fig. 1 Single wall carbon nanotubes. The ends of nanotubes are capped by fullerene hemispheres. (a) armchair nanotube (b) zigzag nanotube, and (c) chiral nanotube.

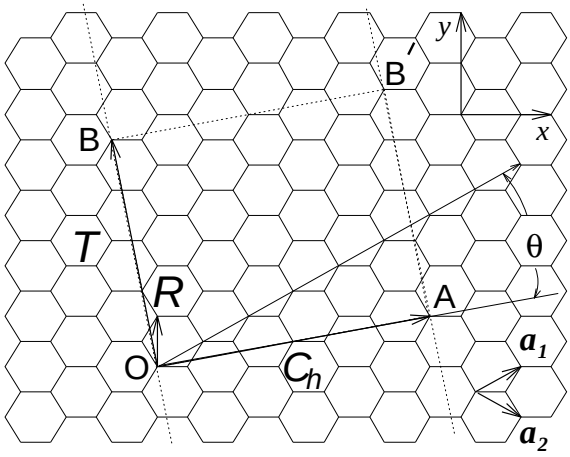

Fig. 2 The unrolled honeycomb lattice of a nanotube. OA is the equator of the nanotube and OB corresponds to the translation vector of this one-dimensional material and OA is the chiral vector. By connecting OB to AB′, we can make a seamless cylindrical shape. OAB′B is a unit cell of the nanotube. The figure corresponds to the (4,2) chiral nanotube and there are $N = 28$ hexagons in the unit cell for this nanotube.

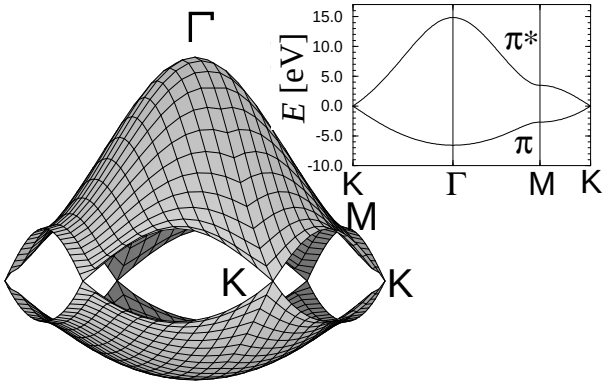

Fig. 3 The energy dispersion relations for 2D graphite are shown throughout the whole region of the Brillouin zone. The inset shows the energy dispersion along the high symmetry points.

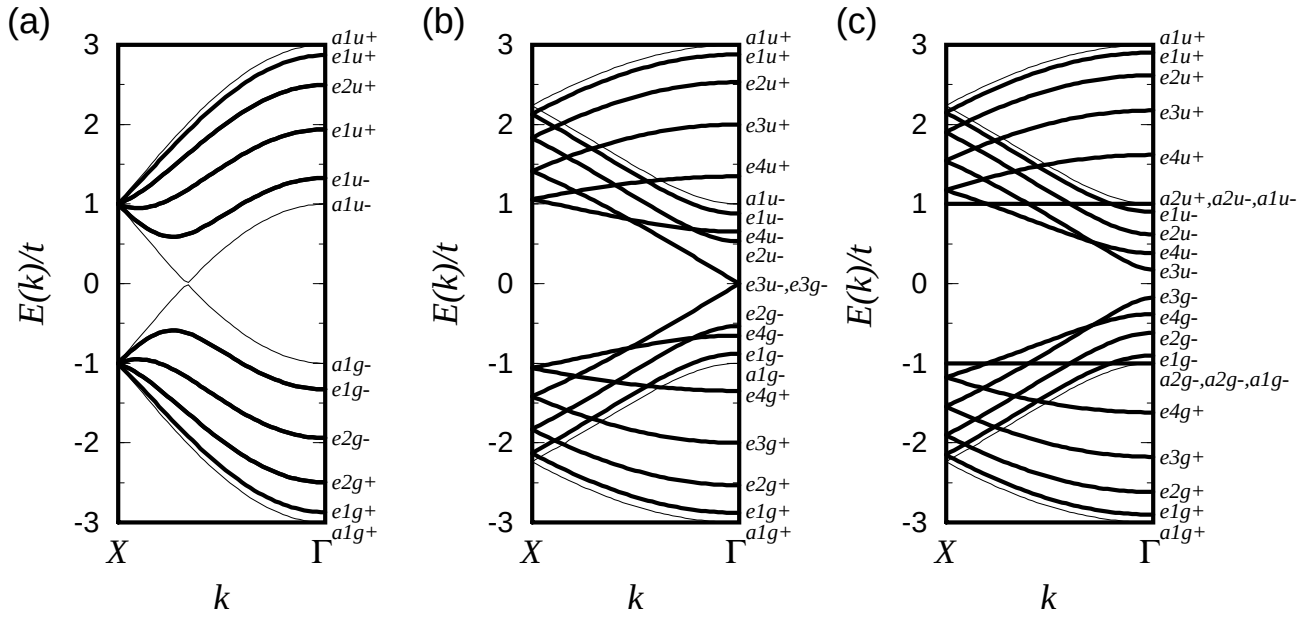

Fig. 4 The energy dispersion relations for carbon nanotubes, shown explicitly for the (a) (5,5) armchair, (b) (9,0) zigzag, (c) (10,0) zigzag nanotubes. Bold and thin lines are doubly or singly degenerate energy bands, respectively. The Fermi energy is located at $E = 0$. (5,5) and (9,0) are metallic nanotubes, while (10,0) is semiconducting.

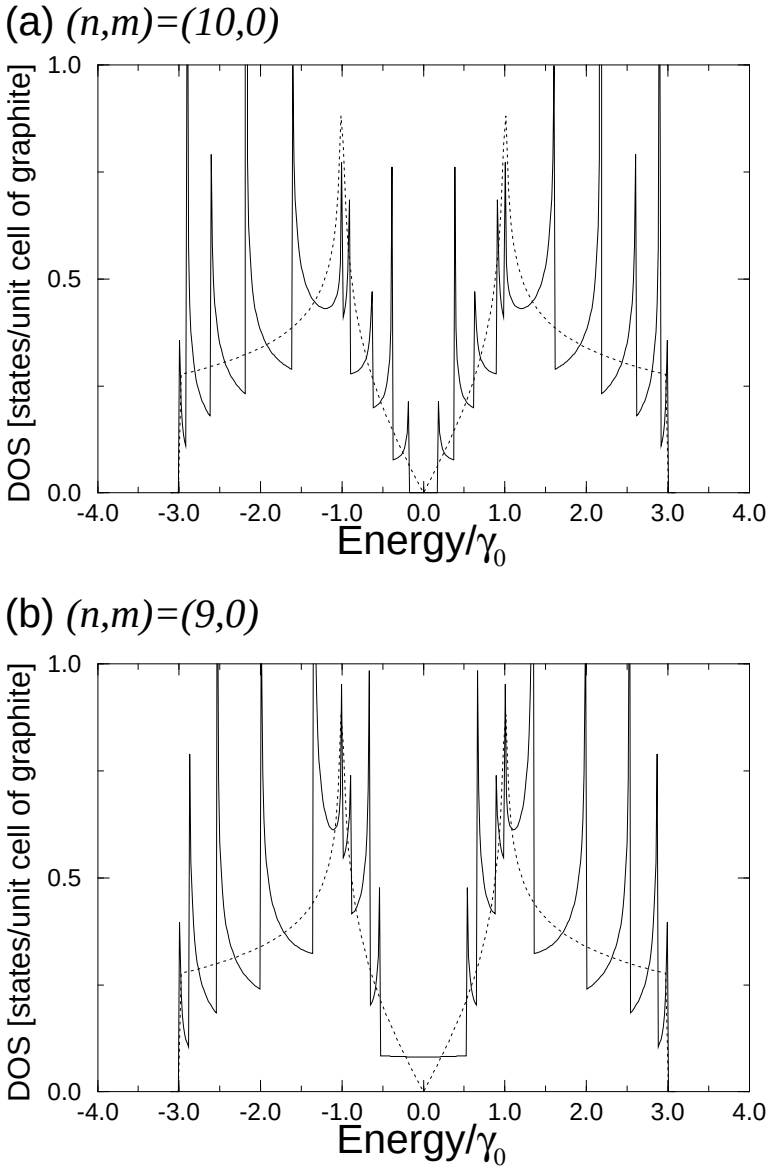

Fig. 5 Electronic density of states for the: (a) (10,0) semiconducting zigzag nanotube, and the (b) (9,0) metallic zigzag nanotube. Dotted lines denote the density of states for two-dimensional graphite.

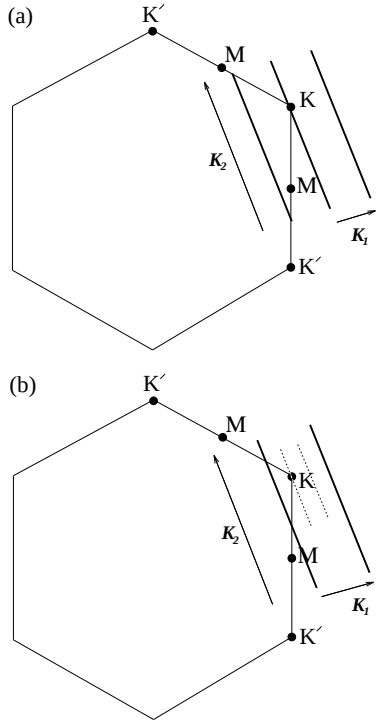

Fig. 6 Cutting lines around the K point in the Brillouin zone for (a) metallic and (b) semiconducting nanotubes.

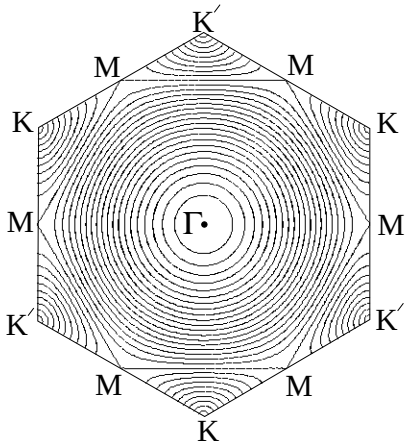

Fig. 7 Equi-energy contours for the electronic π-bands of two-dimensional graphite.

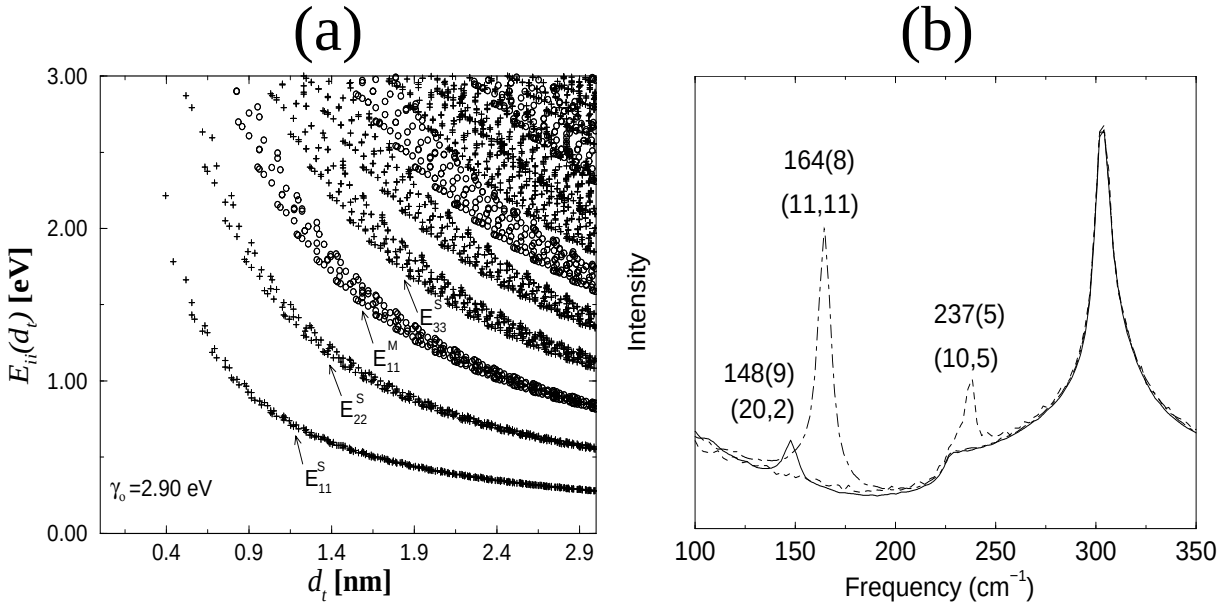

Fig. 8 (a) Energy separations E_{ii} between valence and conduction band Van Hove singularities are plotted as a function of nanotube diameter. (b) Raman spectra (radial breathing mode) from three different (n, m) isolated single wall nanotubes.

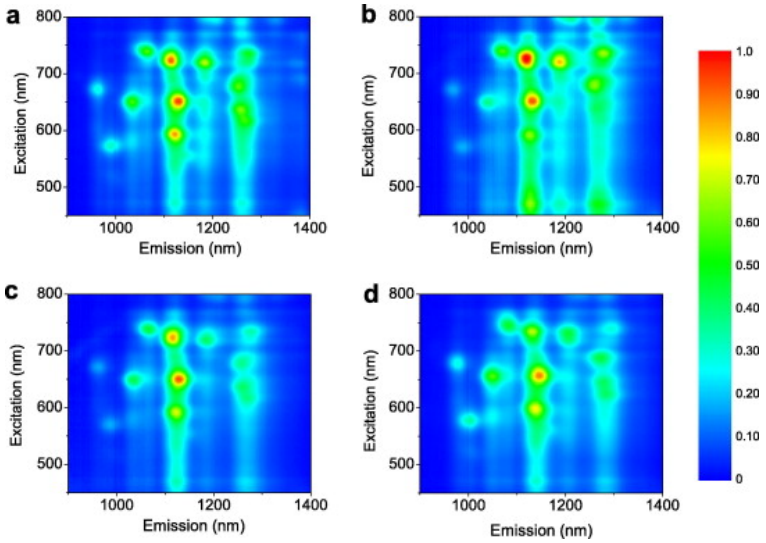

Fig. 9 Photoluminescence excitation (PLE) maps of carbon nanotube samples dispersed in aqueous solution and wrapped with the following chemical moieties: (a) SDS, (b) NaDDBS, (c) NaC, and (d) DNA(GT)10. The same color scale for intensities, normalized to 1, were used in the four plots better visualization.(Reprint from Reference [35]).

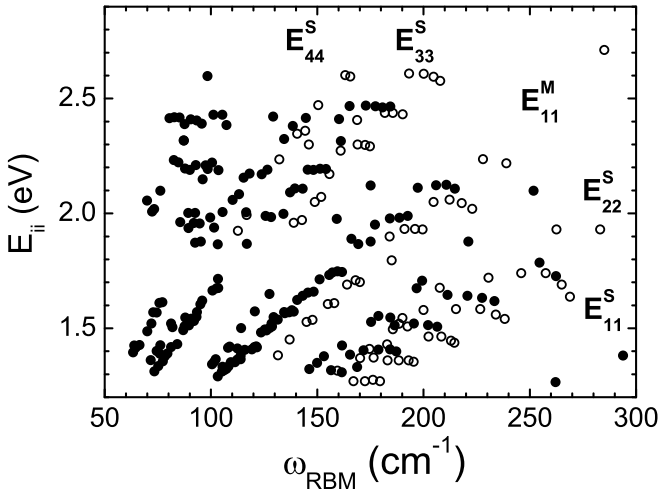

Fig. 10 $E_{ii}^{\rm exp}$ vs. $\omega_{\rm RBM}$ results obtained for the "super-growth" (bullets) and "alcohol assisted" (open circles) SWNT samples.

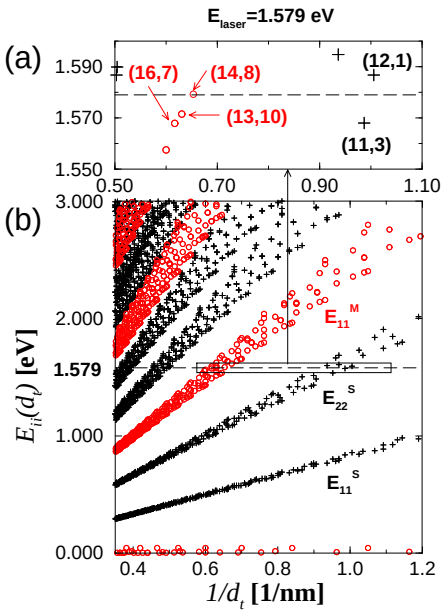

Fig. 11 Van Hove singular energies in the JDOS, E_{ii} as a function of $1/d_t$ are shown in (b) where circles and crosses correspond, respectively, to metallic and semiconducting nanotube with (n, m) chirality tubes. For 1.579 eV laser excitation, expansion of the rectangular section in (b) is shown in (a). The resonance condition satisfies only a limited number of (n, m) tubes whose RBM frequencies can almost always be distinguished from one another.

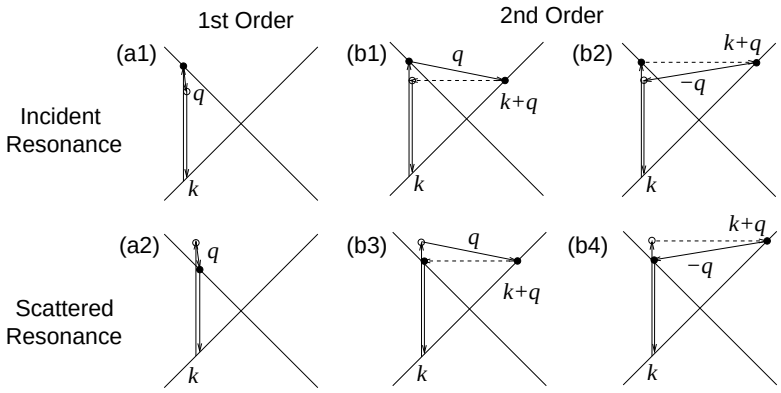

Fig. 12 (a) First-order Raman processes which are resonant with (a1) the incident and (a2) the scattered laser light. Solid and open dots denote resonance and non-resonance scattering processes, respectively. Crossed lines show the linear energy dispersion of 2D graphite around the K point. (b) Second-order Raman processes which are resonant the incident laser light in (b1,b2), and the scattered laser light in (b3,b4). The solid scattered vectors and dashed scattered vectors with wavevector q, respectively, denote inelastic and elastic scattering processes.

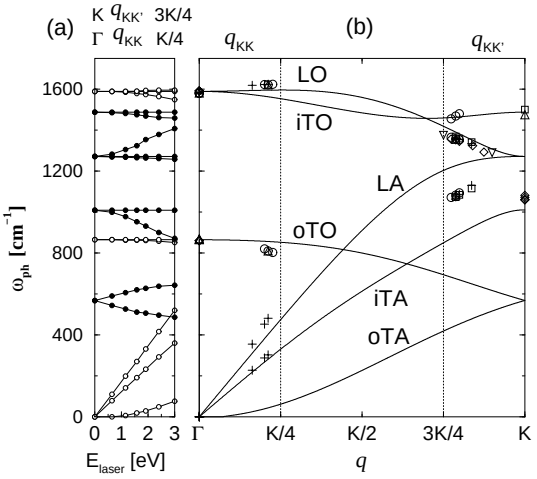

Fig. 13 (a) Calculated Raman frequencies for the double resonance condition as a function of E_{laser} (bottom axis) and q vector along $\Gamma - K$ (top axis). Solid and open circles correspond to phonon modes around the K and Γ points, respectively. (b) The 6 graphite phonon dispersion curves (lines) and experimental Raman observations (symbols) are identified according to double resonance theory.